



# Efficient HCHO oxidation at room temperature via maximizing catalytic sites in 2D coralloid $\delta$ -MnO<sub>2</sub>@GO

Yiheng Li<sup>a,1</sup>, Tao Dong<sup>a,1</sup>, Pingli Huang<sup>a</sup>, Jian Ji<sup>b</sup>, Haibao Huang<sup>a,\*</sup>

<sup>a</sup> School of Environmental Science and Engineering, Sun Yat-sen University, East Waihuan Road, Guangzhou 510006, China

<sup>b</sup> Institute of Chemical Engineering, Guangdong Academy of Sciences, Guangzhou 510665, China

## ARTICLE INFO

### Keywords:

Indoor air pollution  
Formaldehyde catalytic elimination  
 $\delta$ -MnO<sub>2</sub>  
Graphene oxide  
Catalytic site exposure

## ABSTRACT

Airborne formaldehyde (HCHO) in indoor environments causes serious health problems and needs to be efficiently eliminated. However, the efficient and stable catalytic oxidation of HCHO can be hardly achieved at room temperature over transition metal oxides due to the limited exposure of active sites. Herein,  $\delta$ -MnO<sub>2</sub>@GO catalysts were originally synthesized via a facile in situ growth of  $\delta$ -MnO<sub>2</sub> on the trace graphene oxide (GO) substrate (1%) and stably exhibited nearly 100% HCHO elimination at room temperature.  $\delta$ -MnO<sub>2</sub>@GO showed the unique 2D coralloid structure with uniformly dispersed  $\delta$ -MnO<sub>2</sub> nanorod on planar-structured GO, which greatly enhanced the exposure of catalytic sites and mass transfer of reactants. The abundant surface reactive oxygen species (ROS) and hydroxyl (-OH) groups were rapidly generated from the activation of O<sub>2</sub> and surface-adsorbed water over highly exposed catalytic sites. The ROS and -OH groups cooperated well to maintain the exceptional catalytic activity and stability towards HCHO degradation. In-situ DRIFTS results showed that catalytic HCHO oxidation predominantly follows the Langmuir-Hinshelwood (L-H) mechanism over the  $\delta$ -MnO<sub>2</sub>@GO. This study presents a simple yet effective strategy for maximizing exposure to catalytic active sites and rational design of efficient catalysts for indoor HCHO elimination.

## 1. Introduction

Indoor air quality is critical to human health as people spend approximately 90% of their daily time indoors [1]. Formaldehyde (HCHO), classified as a class 1 carcinogen by the International Agency for Research on Cancer (IARC), is widely emitted from the artificial wood-based composites and leathers [2–4]. Even low levels of exposure to HCHO can cause adverse effects on the heart, aorta, and kidneys, and increase the risk of several types of cancer [5]. The permissible exposure limit for formaldehyde set by the U.S. Department of Labor's Occupational Safety and Health Administration is 0.75 ppm [6]. Therefore, the elimination of HCHO is of utmost importance to meet environmental regulations and protect human health. Various techniques have been developed to remove HCHO, such as adsorption, plasma treatment, photocatalytic oxidation, and thermocatalytic oxidation [7–10]. Among them, catalytic oxidation in ambient conditions without the aid of light/heat/electricity has been recognized as the most promising approach [11]. This has been accomplished through the design and development of highly efficient catalysts, including noble and non-noble

metals. Although noble metal catalysts exhibit excellent performance and stability for HCHO oxidation at room temperature, their scarcity and high cost make transition metal oxide catalysts a more favorable choice [12]. Therefore, it is highly desirable to develop efficient and stable transition metal catalysts to eliminate the widespread formaldehyde pollution.

Among the transition metal catalysts, manganite oxides (MnO<sub>x</sub>) often exhibits superior HCHO catalytic oxidation capacity at low temperatures. However, the self-assembled spherical structure of MnO<sub>x</sub> particles easily leads to severe blockage of the pore structures and low exposure of the HCHO adsorption/catalysis sites, so that the mass transfer of the reactants and products are extremely limited [13,14]. This leads to the fact that MnO<sub>x</sub> catalysts can hardly achieve efficient and stable catalytic oxidation of HCHO at room temperature and are easily deactivated [15]. Many studies have shown that the construction of defect sites and hierarchical pore structures are favor to the adsorption, mass transfer, and activation of VOC molecules [16]. In light of this, considerable efforts have been made to tune the geometry and electronic structure of Mn-based catalysts by loading them on various

\* Corresponding author.

E-mail address: [seabao8@gmail.com](mailto:seabao8@gmail.com) (H. Huang).

<sup>1</sup> These authors contributed equally

substrate materials to increase their HCHO adsorption and catalytic site exposure [17,18]. Thereinto, graphene oxide (GO), as an important derivative of graphene, contains sufficient oxygenated functional groups, which are considered as potential adsorption sites and active centers for the construction of multifunctional nanocomposites [19,20]. Li et al [21], observed that GO provides the anchoring sites for MnO<sub>2</sub> deposition and prevents the aggregation of MnO<sub>2</sub> particles. Hu et al [22], found that MnO<sub>2</sub> loading on the GO nanosheet increases the specific surface area and active site of the catalyst, and the synergistic effect between GO and MnO<sub>2</sub> notably improves the catalytic activity of benzyl alcohol to benzaldehyde. Thus, it is feasible to support MnO<sub>2</sub> on GO for HCHO oxidation, which is expected to promote the dispersion and exposure of active sites for enhancing HCHO adsorption/catalytic capability.

In this study, the 2D coralloid hierarchical pore materials were synthesized by in situ growth of  $\delta$ -MnO<sub>2</sub> on the GO substrate ( $\delta$ -MnO<sub>2</sub>@GO). The modification of GO effectively inhibited the excessive growth and agglomeration of  $\delta$ -MnO<sub>2</sub> into large-sized nanospheres. The interaction between GO and MnO<sub>2</sub> promoted the exposure of adsorption/catalytic active sites and the mass transfer efficiency of the reactants and products. Additionally, a series of in situ DRIFTS experiments were performed to study the reaction mechanism of HCHO oxidation. It was shown that the abundant oxygen vacancy of  $\delta$ -MnO<sub>2</sub>@GO-RT rapidly converted the adsorbed water into the surface -OH groups. The surface -OH groups and ROS synergistically reduced the accumulation of intermediates, and that HCHO oxidation follows the L-H mechanism. The strategy of maximizing the exposure of the catalytic active sites enlightens the rational design of efficient catalysts and paves the way for their widespread application in indoor HCHO abatement.

## 2. Materials and methods

### 2.1. Catalyst preparation

First, GO was synthesized by a modification of Hummer's method [23]. Then, the optimal calculated amount of GO, accounting for 1% of the total catalyst, along with 0.28 g of MnSO<sub>4</sub>·H<sub>2</sub>O (Aladdin) and 1.50 g KMnO<sub>4</sub> (Tianjin wind boat chemical reagent Technology Co., Ltd.), was added to 80 mL of deionized water. The mixture was subjected to magnetic stirring for 30 min and aged at room temperature for 12 h to ensure complete reaction. The obtained precipitate was washed with deionized water by centrifugation until the supernatant became colorless and transparent. Then, the precipitate was freeze-dried at -80 °C for 3 days and named  $\delta$ -MnO<sub>2</sub>@GO-RT. The catalyst prepared by the hydrothermal method is named  $\delta$ -MnO<sub>2</sub>@GO-HT. In addition, the catalyst prepared by industrial GO powder (XFNANO Co., Ltd.) is named  $\delta$ -MnO<sub>2</sub>@GO-RT-I. The reference catalysts (i.e.,  $\delta$ -MnO<sub>2</sub>-RT,  $\delta$ -MnO<sub>2</sub>@GO-HT,  $\delta$ -MnO<sub>2</sub>-HT,  $\delta$ -MnO<sub>2</sub>@GO-RT-I) were produced in the similar processes and the detailed preparation methods were described in the [Supplementary Information](#).

### 2.2. Catalyst characterization

X-ray diffraction (XRD), field emission scanning electron microscopy (FE-SEM), high resolution transmission electron microscopy (HRTEM), Raman spectra, X-ray photoelectron spectroscopy (XPS), N<sub>2</sub> adsorption/desorption analysis, H<sub>2</sub> temperature programmed reduction (H<sub>2</sub>-TPR), O<sub>2</sub> temperature programmed desorption (O<sub>2</sub>-TPD), HCHO temperature programmed desorption (HCHO-TPD), and in situ diffuse reflectance infrared Fourier transform spectroscopy (in situ DRIFTS) characterization tests were used to characterize and predict the physical and chemical properties and possible reaction mechanisms of  $\delta$ -MnO<sub>2</sub>@GO-RT and related catalysts. The details of characterization methods are presented in [Supplementary Information](#).

## 3. Results and discussion

### 3.1. Synthesis and morphological structure of catalysts

The 2D coralloid  $\delta$ -MnO<sub>2</sub>@GO was synthesized by in situ growth of  $\delta$ -MnO<sub>2</sub> on GO substrates, as illustrated in Fig. 1a. SEM images in Fig. 1b1-b2 showed rough and irregular nanorods of the  $\delta$ -MnO<sub>2</sub>-RT, which agglomerated into flower-like microspheres. Upon the modification of GO, the microsphere structure transforms into a planar structure, as shown in Fig. 1c1-c2 ( $\delta$ -MnO<sub>2</sub>@GO-RT). The EDS Mapping (Fig. S1) confirmed the uniform distribution of Mn, O, and K species on the carbon substrates, indicating the in-situ formation of  $\delta$ -MnO<sub>2</sub> nanorods on GO substrates. Additionally, the influence of hydrothermal treatment on the morphology and structure of the  $\delta$ -MnO<sub>2</sub> material was investigated (Figs. 1d and 1e). The flower-like microsphere structure of  $\delta$ -MnO<sub>2</sub>-HT cross-linked by nanosheets is observed in Fig. 1d1-d2. Similarly, with the modification of GO, the flower-like microsphere structure is transformed into a planar structure ( $\delta$ -MnO<sub>2</sub>@GO-HT), as shown in Fig. 1e1-e2. The magnified images of  $\delta$ -MnO<sub>2</sub>@GO-RT (Fig. 1 c2) showed nanorods crisscrossing across a flat surface, like the tentacles of an anemone. In comparison, the magnified images of  $\delta$ -MnO<sub>2</sub>@GO-HT (Fig. 1 e2) presented a hierarchical and intersecting microstructure with a smaller distance between two adjacent nanosheets than that of  $\delta$ -MnO<sub>2</sub>-HT. Based on these observations, possible growth mechanisms can be suggested. First, Mn<sup>2+</sup> ions electrostatically bind to O atoms of oxygen-containing functional groups on GO planes [24]. Subsequently, MnO<sub>4</sub><sup>-</sup> ions react with the Mn<sup>2+</sup> ions to form abundant nuclei densely attached to the GO planes. Finally, the crystal nuclei were gradually grown into  $\delta$ -MnO<sub>2</sub> nanorods at room temperature while into larger and angular nanosheets during hydrothermal synthesis reaction.

TEM and HRTEM were further measured to evaluate the surface microstructure of the related catalysts. As shown in Fig. 1b3-b4, the structure of  $\delta$ -MnO<sub>2</sub>-RT appeared to be a loose ball with nanorods extending from the edges, while that of  $\delta$ -MnO<sub>2</sub>-HT (Fig. 1d3-d4) was observed to be a mixture of relatively smooth and flat fragments and wedge-shaped nanoplates. Lichen-like structures are observed in both  $\delta$ -MnO<sub>2</sub>@GO-RT (Fig. 1c3-c4) and  $\delta$ -MnO<sub>2</sub>@GO-HT (Fig. 1e3-e4), with the latter being darker, indicating that hydrothermal reactions contributed to the thickness of the catalyst. The lattice spacings of 0.71 nm and 0.24 nm, corresponding to the (0 0 1) and (1 0 0) facets of  $\delta$ -MnO<sub>2</sub>, can be clearly observed in  $\delta$ -MnO<sub>2</sub>-HT and  $\delta$ -MnO<sub>2</sub>@GO-HT [25]. However,  $\delta$ -MnO<sub>2</sub>-RT and  $\delta$ -MnO<sub>2</sub>@GO-RT had no clear lattice spacing. Therefore, the hydrothermal method might make the structure of the material smoother and more regular and reduce the surface defects, which may have a negative effect on the catalytic activity.

The X-ray diffraction (XRD) patterns of the catalysts (Fig. 2a) displayed diffraction peaks at 12.3°, 36.8°, and 65.7°, corresponding to the (002), (006), and (119) crystal planes of hexagonal birnessite MnO<sub>2</sub> (JCPDS 18-0802). It can be observed that  $\delta$ -MnO<sub>2</sub>-HT and  $\delta$ -MnO<sub>2</sub>@GO-HT displayed clearer and stronger diffraction peaks than those synthesized at room temperature. The catalysts prepared at room temperature showed an amorphous state, and the hydrothermal treatment increased the crystallinity of catalysts. The diffraction peak at 24.8° corresponded to the (006) crystal plane of monoclinic potassium birnessite MnO<sub>2</sub> (JCPDS 86-0666), suggesting the introduction of K<sup>+</sup> ions from potassium permanganate. With the addition of GO, the peak intensities of  $\delta$ -MnO<sub>2</sub>@GO-HT are slightly weaker than those of  $\delta$ -MnO<sub>2</sub>-HT, indicating reduced crystallinity and formation of a new structure, consistent with the results of SEM. However, no diffraction peaks of GO are observed, probably due to the low GO loading. Raman spectra were performed to analyze the bonding structure of the surface atoms in the  $\delta$ -MnO<sub>2</sub> catalysts (Fig. 2b). All catalysts exhibited three similar characteristic peaks at 499–508 cm<sup>-1</sup>, 557–577 cm<sup>-1</sup>, and 618–637 cm<sup>-1</sup>. The band at 577 cm<sup>-1</sup> is attributed to the  $\nu_2$ (Mn-O) stretching vibration in the basal plane of MnO<sub>6</sub> sheets, and the bands at 637 cm<sup>-1</sup> and 636 cm<sup>-1</sup> corresponded to the  $\nu_3$ (Mn-O) symmetric stretching vibration



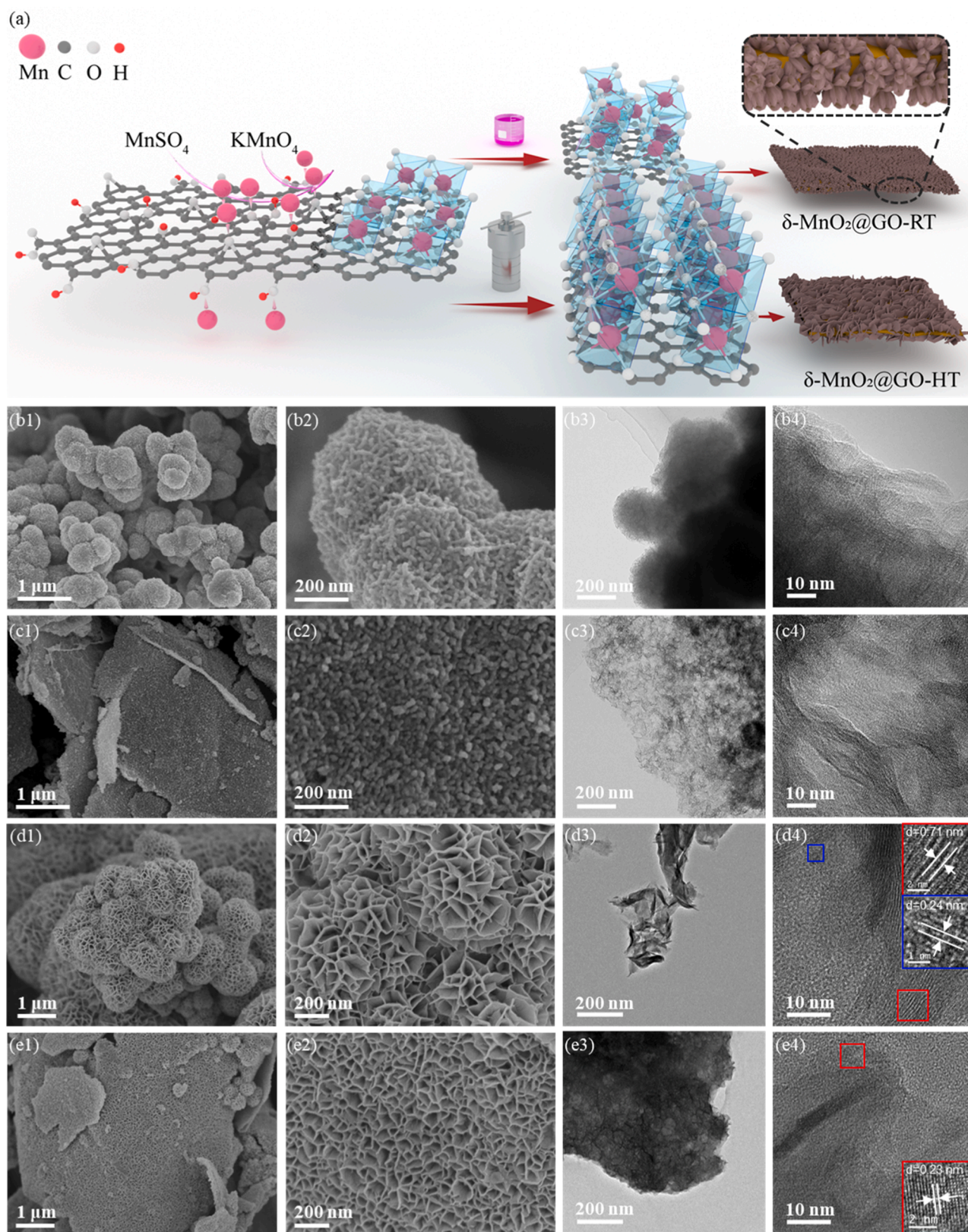


**Fig. 1.** Schematic illustration of the synthetic route of various  $\delta$ -MnO<sub>2</sub> catalysts (a) and FESEM, TEM and HRTEM images of (b1-b4)  $\delta$ -MnO<sub>2</sub>-RT, (c1-c4)  $\delta$ -MnO<sub>2</sub>@GO-RT, (d1-d4)  $\delta$ -MnO<sub>2</sub>-HT, (e1-e4)  $\delta$ -MnO<sub>2</sub>@GO-HT.

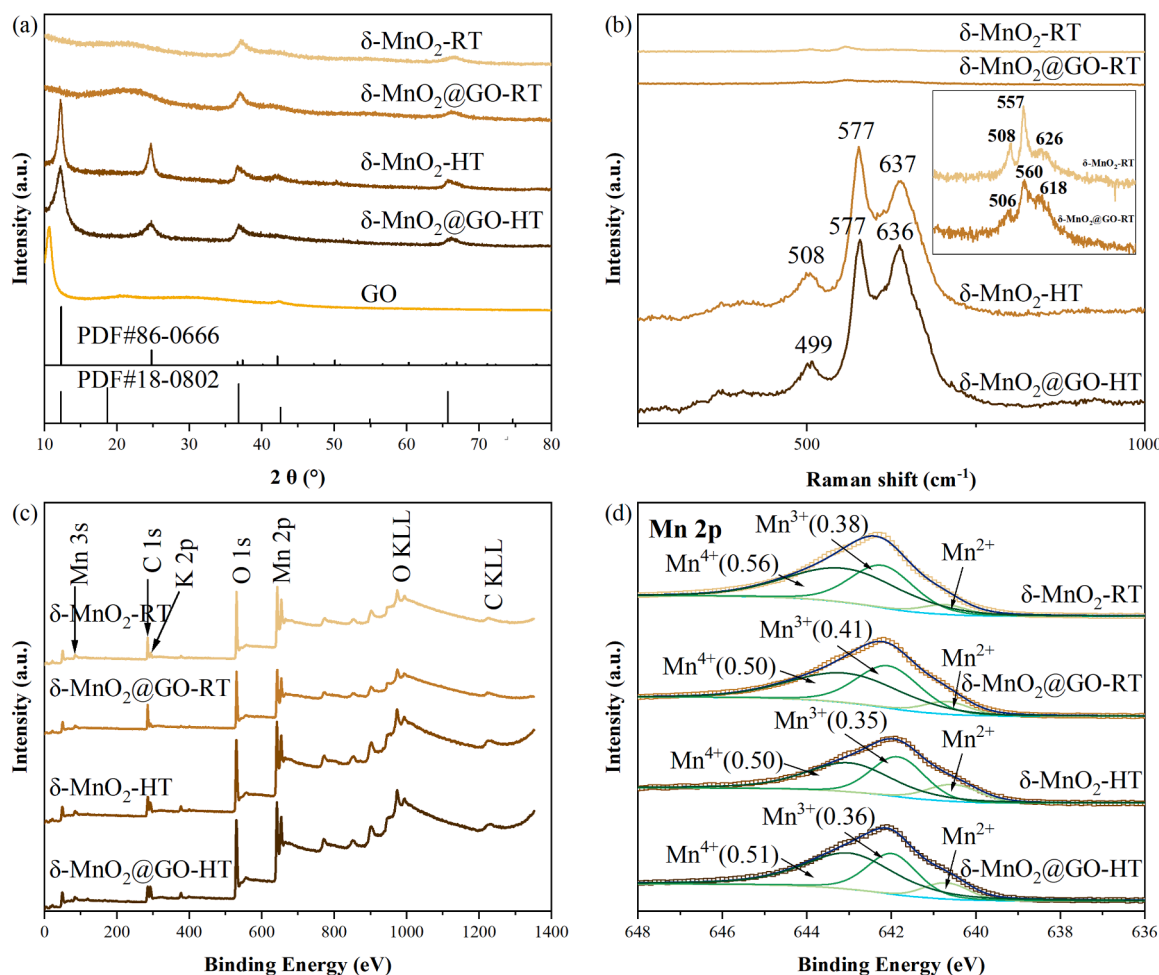


**Fig. 2.** (a) XRD patterns of various  $\delta\text{-MnO}_2$  and GO samples, (b) Raman spectra of various  $\delta\text{-MnO}_2$  samples from 200 to 1000  $\text{cm}^{-1}$  (the inset displayed the magnified Raman spectra of  $\delta\text{-MnO}_2\text{-RT}$  and  $\delta\text{-MnO}_2\text{@GO-RT}$ ), and XPS spectra of various  $\delta\text{-MnO}_2$  samples: (c) survey spectrum and (d) Mn 2p spectrum.

of the  $[\text{MnO}_6]$  groups [26,27]. The intensity of the peaks over  $\delta\text{-MnO}_2\text{@GO-RT}$  are weaker than  $\delta\text{-MnO}_2\text{-RT}$  and the peak positions have been slightly redshifted, proving that the introduction of GO weakened the strength of the Mn-O bond. The Mn-O bond force constant ( $k$ ), which represents the bond strength, was calculated using Hooke's law (details of the calculation are provided in the Supplementary Information) [28]. The calculated order of the Mn-O bond force constant ( $k$ ) is as follows:  $\delta\text{-MnO}_2\text{-HT}$  (1.933 N/m) >  $\delta\text{-MnO}_2\text{@GO-HT}$  (1.926 N/m) >  $\delta\text{-MnO}_2\text{-RT}$  (1.866 N/m) >  $\delta\text{-MnO}_2\text{@GO-RT}$  (1.819 N/m). Notably, the force constant ( $k$ ) of  $\delta\text{-MnO}_2\text{@GO-RT}$  is the lowest, indicating the loosest Mn-O bond with a tendency for oxygen atoms to escape and form oxygen vacancies. Combined with the SEM, TEM, XRD, and Raman results, it can be suggested that the  $\delta\text{-MnO}_2$  samples synthesized at room temperature had more defect sites compared to those synthesized by the hydrothermal treatment.

XPS was performed to investigate the surface elemental state of various  $\delta\text{-MnO}_2$  samples. As shown in Fig. 2c, all samples exhibited the presence of Mn, O and K elements. The Mn 2p spectrum displayed three distinct components centered around 640.5 eV, 642 eV, and 643 eV, corresponding to  $\text{Mn}^{2+}$ ,  $\text{Mn}^{3+}$ , and  $\text{Mn}^{4+}$ , respectively (Fig. 2d). The  $\delta\text{-MnO}_2\text{@GO-RT}$  had the biggest value of the  $\text{Mn}^{3+}$  ratio (0.48) among all samples, demonstrating the most oxygen vacancy and active sites [24].

### 3.2. Catalytic oxidation of HCHO at room temperature

The catalytic oxidation performance of HCHO was tested at room

temperature (25 °C). As shown in Fig. 3a, all catalysts exhibited remarkable HCHO removal efficiency, which reached nearly 100% in the initial stage of 130 min. As the reaction proceeded, HCHO removal efficiency of  $\delta\text{-MnO}_2\text{-HT}$ ,  $\delta\text{-MnO}_2\text{@GO-HT}$  and  $\delta\text{-MnO}_2\text{-RT}$  started to decrease after 130 min, 190 min, and 240 min to reach 17%, 30%, and 61%, respectively. In contrast, HCHO removal efficiency of  $\delta\text{-MnO}_2\text{@GO-RT}$  remained stable, maintaining a maximum value of 100% in 400 min.  $\delta\text{-MnO}_2\text{@GO-RT}$  showed excellent catalytic oxidation performance of HCHO compared to other relevant studies (Table S1). Furthermore, Fig. 3b illustrates that the generated  $\text{CO}_2$  concentrations are more stable for  $\delta\text{-MnO}_2\text{@GO-RT}$  compared with the other three samples. This suggests that  $\delta\text{-MnO}_2\text{@GO-RT}$  can continuously convert HCHO to  $\text{CO}_2$  due to the exposure of abundant active sites. The HCHO elimination rate to be maintained at 100% is extended by 100 min ( $\delta\text{-MnO}_2\text{-RT}$ ) and 200 min ( $\delta\text{-MnO}_2\text{@GO-RT}$ ), respectively, showing the enhanced stability compared to  $\delta\text{-MnO}_2\text{-HT}$  and  $\delta\text{-MnO}_2\text{@GO-HT}$ . It can be attributed to the weaker Mn-O bond in the catalysts prepared at room temperature, which leads to the generation of more defect sites and accelerates the activation of reactants [29,30].

The influence of humidity on the catalytic activity of HCHO oxidation was investigated since water is ubiquitous in ambient air and plays a vital role in HCHO oxidation. As shown in Fig. 3c, the HCHO oxidation performance of  $\delta\text{-MnO}_2\text{@GO-RT}$  was optimal at a relative humidity (RH) of 50%. As the humidity decreased, the concentration of  $\text{CO}_2$  from HCHO oxidation decreased from 37 ppm to 22 ppm and finally stabilized at 6 ppm (Fig. 3d). The decrease in RH resulted in insufficient adsorbed water on the catalyst surface to generate surface -OH groups,



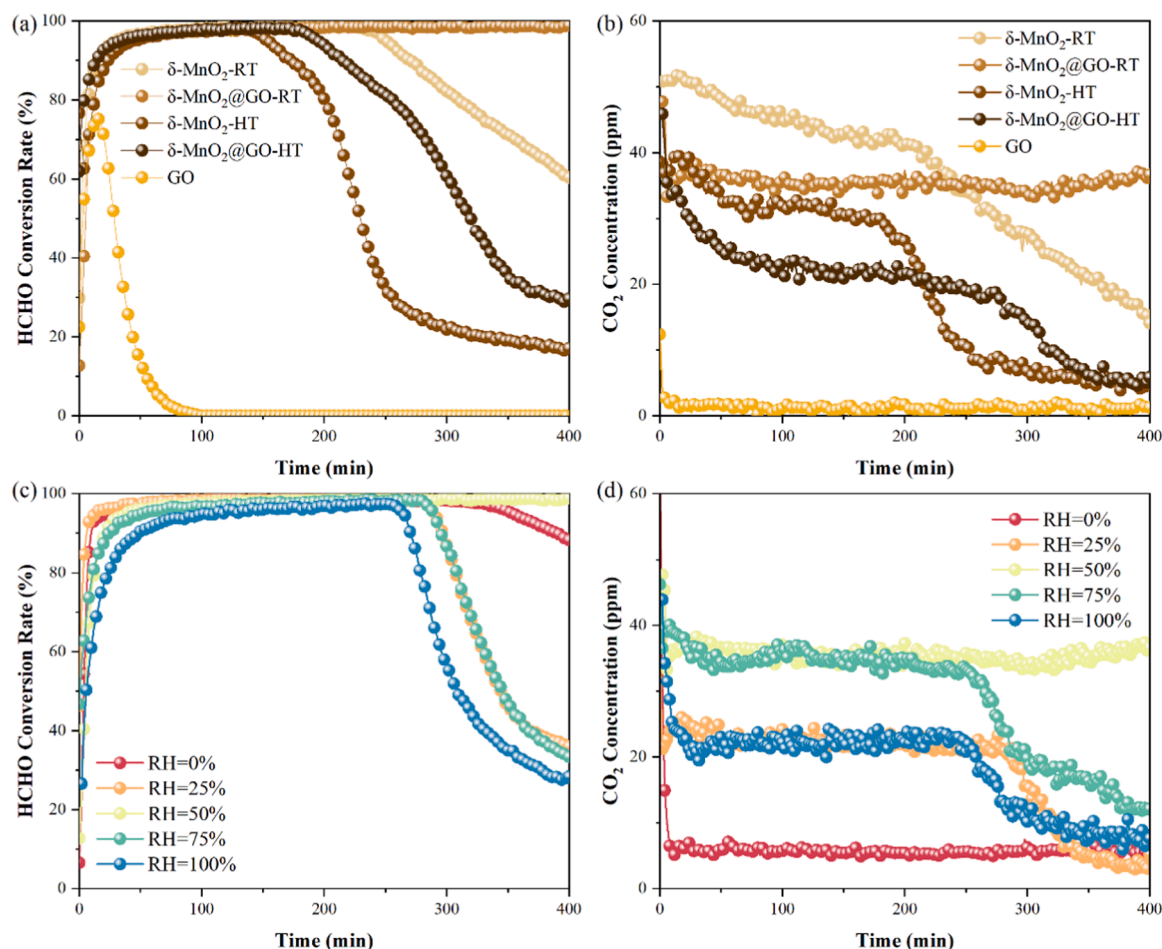


**Fig. 3.** (a) HCHO removal efficiency and (b) corresponding CO<sub>2</sub> concentration as a function of time over δ-MnO<sub>2</sub> and δ-MnO<sub>2</sub>@GO samples (HCHO concentration = 100 ppm, air as balance gas, temperature ~ 25 °C, RH = 50%, GHSV = 72 L/g<sub>cat</sub>·h); (c) HCHO removal efficiency and (d) corresponding CO<sub>2</sub> concentration as a function of time over δ-MnO<sub>2</sub>@GO-RT at different relative humidity. (RH = 0%, 25%, 50%, 75%, and 100%).

leading to a decline in HCHO oxidation performance. Similarly, as the RH increased, the activity and stability of HCHO oxidation over δ-MnO<sub>2</sub>@GO-RT also decreased. This can be attributed to excessive water molecules occupying active sites owing to the competitive adsorption between water and HCHO [31]. The HCHO catalytic oxidation performance of δ-MnO<sub>2</sub>@GORT and δ-MnO<sub>2</sub>@GOHT (Fig. S5) were much better compared to that of δ-MnO<sub>2</sub>-RT and δ-MnO<sub>2</sub>-HT under different humidity conditions (Fig. S3 and S4), respectively, confirming that the modification of GO improved the water utilization of the catalysts.

### 3.3. Analysis of the essential reason of superior catalytic performance

In order to identify the essential reason for the optimal HCHO oxidation performance over δ-MnO<sub>2</sub>@GO-RT, various characterization techniques were performed. N<sub>2</sub> adsorption-desorption isotherms and pore size distribution curves are shown in Fig. S6a and b. All isotherms exhibit type IV with type H3 hysteresis loops, proving the presence of irregular slit-like mesopores. The BET surface area values (Table S2) of δ-MnO<sub>2</sub>-RT, δ-MnO<sub>2</sub>-HT, δ-MnO<sub>2</sub>@GO-HT and GO are 14, 23, 39, and 39 m<sup>2</sup>g<sup>-1</sup>, respectively. However, the specific surface area of δ-MnO<sub>2</sub>@GO-RT reached a high value of 185 m<sup>2</sup>g<sup>-1</sup>. It is suggested that the GO can provide growth sites for δ-MnO<sub>2</sub> dispersion, which effectively controlled the overgrowth of δ-MnO<sub>2</sub> particles. At the same time, the modification of GO changed the surface properties of δ-MnO<sub>2</sub> and prevented the agglomeration of δ-MnO<sub>2</sub> [32]. The interaction between GO and MnO<sub>2</sub> promoted the exposure of active sites and the

improvement of the mass transfer efficiency of the reactants.

To confirm that the mass transfer effect of HCHO molecules is enhanced on δ-MnO<sub>2</sub>@GO-RT, we investigated the diffusion behaviour of the HCHO molecule in the relevant samples. The diffusion type is an important factor affecting the mass transfer of HCHO molecules. The Knudsen number can be used to determine the type of molecular diffusion within the pore and can be calculated as follows:

$$K_n = \frac{\lambda}{r}$$

where  $\lambda$  represents the mean free path,  $r$  denotes the pore diameter. When  $K_n \gg 1$ , it corresponds to Knudsen diffusion. According to the calculations, the mean free path of HCHO molecules is 146 nm, resulting in  $K_n \geq 32.44 \gg 1$ . In other words, the diffusion type of formaldehyde molecules in the four catalysts channels belongs to Knudsen diffusion. In this case, molecular collisions can be neglected, and all momentum transfer occurs at the pore wall. According to previous literature, the Knudsen coefficient for a fixed aperture increases with increasing pore length, however, it tends to a constant value as soon as the pore size exceeds a critical length [33]. The pore length of the catalyst reaches this critical value, meaning that the collision probability between formaldehyde molecules and the pore wall no longer increases. Consequently, numerous active sites deeply located inside the pore cannot be effectively utilized [33]. As shown in Fig. S6d and S6f, the lamellar thicknesses of δ-MnO<sub>2</sub>@GO-RT and δ-MnO<sub>2</sub>@GO-HT were 75 nm and 94 nm, respectively, which were much smaller than the observed mean particle sizes of δ-MnO<sub>2</sub>-RT (350 nm) and δ-MnO<sub>2</sub>-HT (740 nm). The

homogeneous dispersion of  $\delta$ -MnO<sub>2</sub> particles on the GO substrate greatly shortened the diffusion distance of HCHO molecules to the active sites. Furthermore, the unavailable active sites in the center of the flower-like sphere are exposed, and the diffusion and migration paths of HCHO molecules are shortened to overcome the diffusion limitation, which significantly improved the catalytic oxidation performance of  $\delta$ -MnO<sub>2</sub>@GO-RT and  $\delta$ -MnO<sub>2</sub>@GO-HT [34].

H<sub>2</sub>-TPR test was also performed to investigate the reducibility of the catalysts. The reduction process of the MnO<sub>2</sub> catalyst typically involves a two-step transition from (i) Mn<sup>4+</sup> to Mn<sup>3+</sup> and (ii) Mn<sup>3+</sup> to Mn<sup>2+</sup>, corresponding to the first and second reduction peaks, respectively [35]. As shown in Fig. 4a, upon the modification of GO, the reduction peaks of  $\delta$ -MnO<sub>2</sub> @GO catalysts shifted towards lower temperature. For  $\delta$ -MnO<sub>2</sub>@GO-RT, the first reduction peak shifted significantly from 322 °C to 276 °C. For  $\delta$ -MnO<sub>2</sub>@GO-HT, the first reduction peak shifted from 277 °C to 270 °C, and the second peak shifted from 311 °C to 303 °C. For GO samples, only a sharp reduction peak at 202 °C can be attributed to the reduction of oxygen-containing functional groups on the GO surface. Interestingly, the reduction peak over  $\delta$ -MnO<sub>2</sub>@GO-RT and  $\delta$ -MnO<sub>2</sub>@GO-HT started to appear at 145 °C and 161 °C, respectively, which may be attributed to the surface-adsorbed oxygen species [36]. These results indicated that the modification of GO facilitated the reductive ability of  $\delta$ -MnO<sub>2</sub> [37].

To investigate the different types of oxygen species presented in the catalysts, O<sub>2</sub>-TPD-MS and XPS of O1s were performed. As shown in O<sub>2</sub>-TPD-MS spectra (Fig. 4b), for  $\delta$ -MnO<sub>2</sub>-RT and  $\delta$ -MnO<sub>2</sub>@GO-RT, the first desorption peak is located at about 500 °C, and another desorption peak is located at about 740 °C. The two desorption peaks are located at about 360 °C and 770 °C over  $\delta$ -MnO<sub>2</sub>-HT and  $\delta$ -MnO<sub>2</sub>@GO-HT. The GO

sample shows a sharp desorption peak at 191 °C, which is probably attributed to the self-decomposition of oxygen-containing functional groups on the GO surface. The desorption peaks observed at temperatures below 400 °C are associated with the desorption of surface chemisorbed O<sub>2</sub>, and those between 400 °C and 600 °C correspond to the desorption of surface chemisorbed O<sup>-</sup>. Peaks above 600 °C are regarded as lattice oxygen species [38,39]. Surface chemisorbed oxygen species play a crucial role in the catalytic decomposition of HCHO at room temperature, and the integrated area of surface chemisorbed oxygen species over four catalysts was in this order:  $\delta$ -MnO<sub>2</sub>-RT ( $1.16 \times 10^{-6}$ ) >  $\delta$ -MnO<sub>2</sub> @GO-RT ( $7.53 \times 10^{-7}$ ) >  $\delta$ -MnO<sub>2</sub> @GO-HT ( $4.66 \times 10^{-7}$ ) >  $\delta$ -MnO<sub>2</sub>-HT ( $4.28 \times 10^{-7}$ ). The intensity of the surface oxygen reduction peaks in  $\delta$ -MnO<sub>2</sub>-RT and  $\delta$ -MnO<sub>2</sub> @GO-RT is higher and the integrated area was larger, indicating that the catalysts prepared at room temperature could release a greater abundance of surface oxygen species. Notably, as shown in the magnified O<sub>2</sub>-TPD-MS spectra from 0 ° to 300 °C (Fig. 4b), all four catalysts showed weak signals in the low temperature range:  $\delta$ -MnO<sub>2</sub>-RT (235 °C),  $\delta$ -MnO<sub>2</sub>@GO-RT (150 °C),  $\delta$ -MnO<sub>2</sub>-HT (197 °C) and  $\delta$ -MnO<sub>2</sub>@GO-HT (178 °C). The surface oxygen species of  $\delta$ -MnO<sub>2</sub>@GO-RT are the easiest to escape due to the lowest temperature of the characteristic peak. The desorption of water in the O<sub>2</sub>-TPD process (Fig. S7) showed that  $\delta$ -MnO<sub>2</sub>@GO-RT has the highest adsorption capacity for water molecules and the strongest hydrophilicity among the investigated catalysts. The XPS spectra of O 1s in Fig. 4c were fitted into three peaks centered around 529.8 eV, 531.4 eV, and 533.1 eV, respectively, corresponding to lattice oxygen (O<sub>latt</sub>), surface adsorbed oxygen species (O<sub>ads</sub>), and adsorbed molecular H<sub>2</sub>O (O<sub>water</sub>) [40]. The order of the O<sub>ads</sub> fraction O<sub>ads</sub>/ (O<sub>latt</sub> + O<sub>ads</sub> + O<sub>water</sub>) in various  $\delta$ -MnO<sub>2</sub> samples is as follows:  $\delta$ -MnO<sub>2</sub> @GO-RT (0.48)

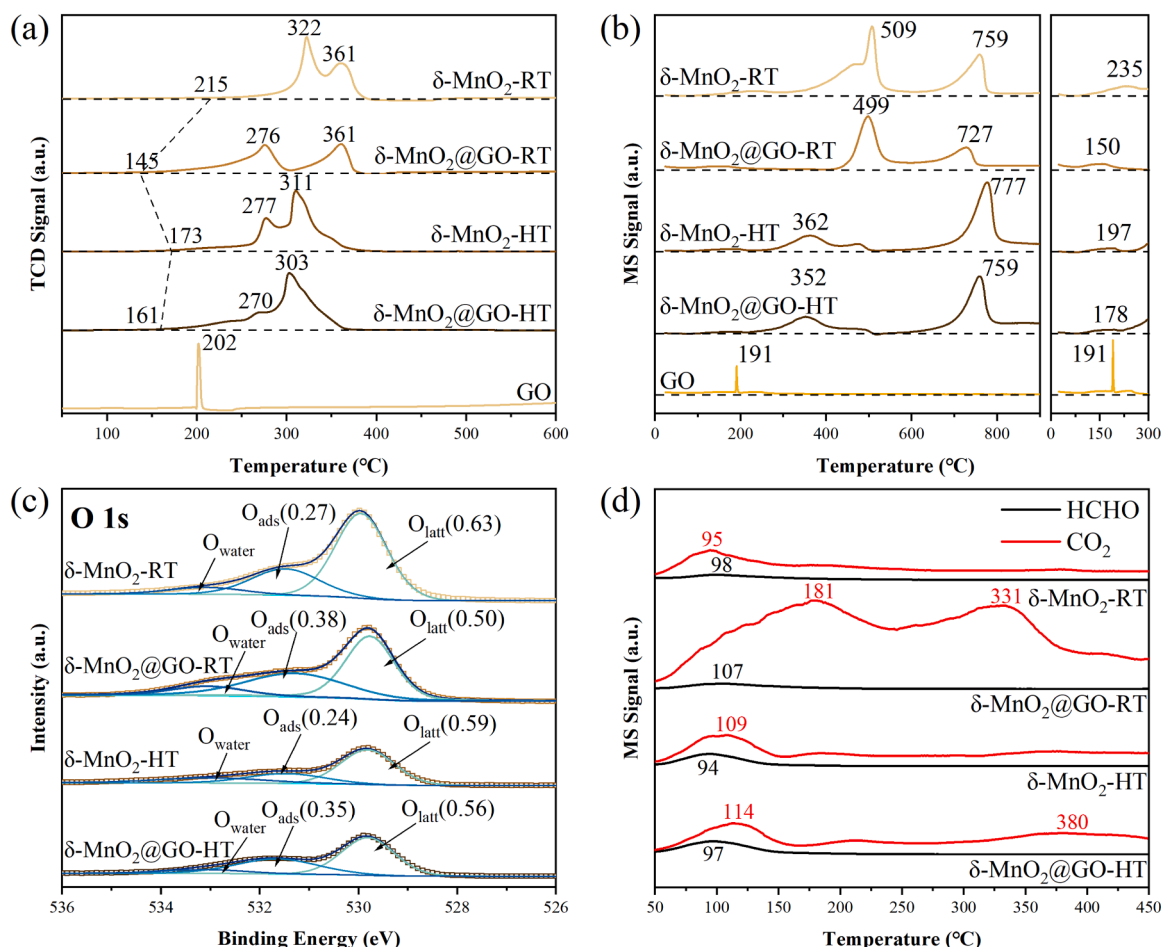
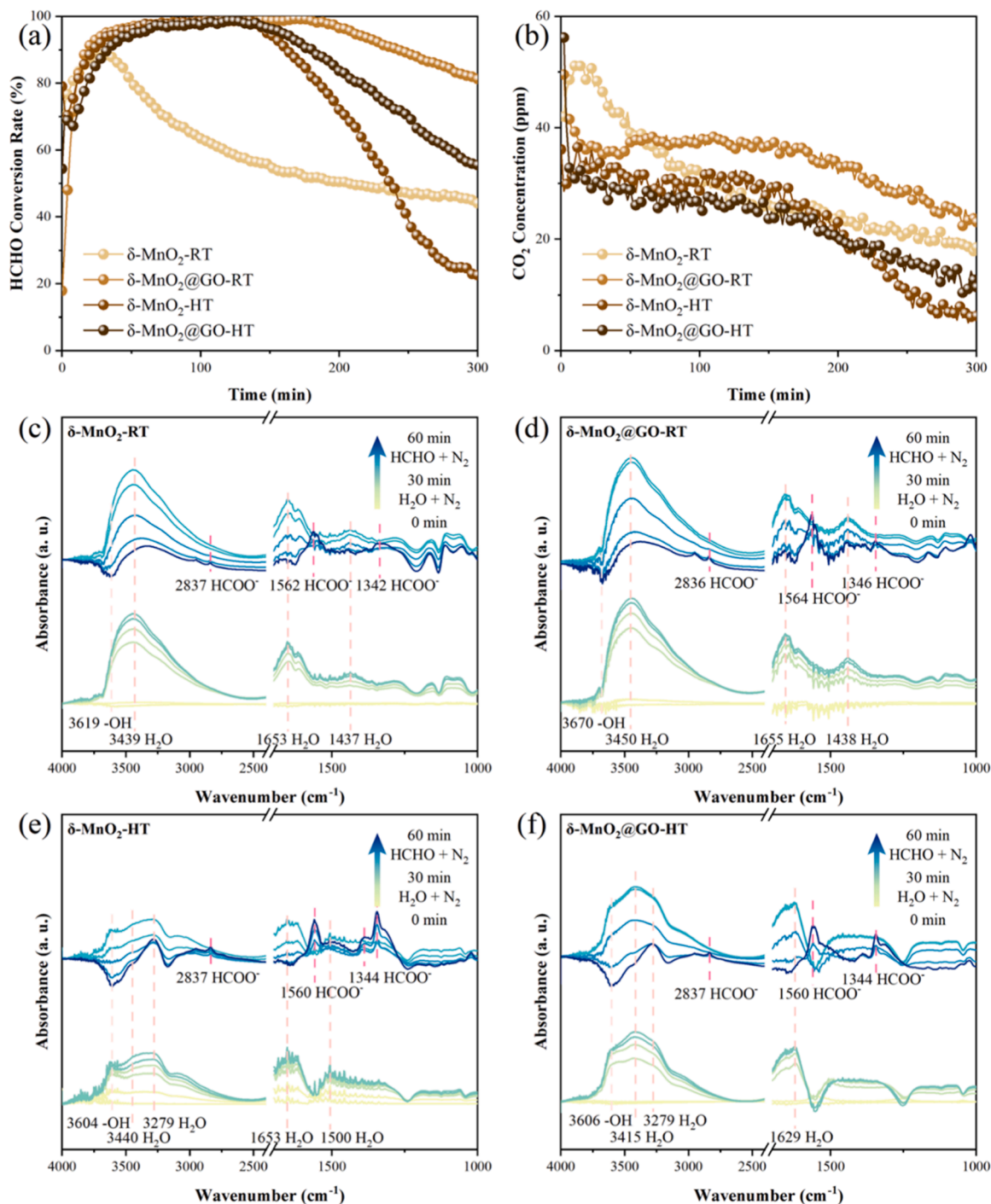


Fig. 4. (a) H<sub>2</sub>-TPR spectra, (b) O<sub>2</sub>-TPD-MS spectra of various  $\delta$ -MnO<sub>2</sub> and GO samples, (c) O1s spectra and (d) HCHO-TPD-MS spectra of various  $\delta$ -MnO<sub>2</sub> samples.

>  $\delta\text{-MnO}_2\text{@GO-HT}$  (0.35) >  $\delta\text{-MnO}_2\text{-RT}$  (0.27) >  $\delta\text{-MnO}_2\text{-HT}$  (0.24). Numerous previous studies have extensively investigated the fraction of  $\text{O}_{\text{ads}}$  as an important indicator of oxygen vacancy concentration. The calculated results reveal that  $\delta\text{-MnO}_2\text{@GO-HT}$  has the highest capability of oxygen vacancy formation among the samples. The fraction of  $\text{O}_{\text{ads}}$  in  $\delta\text{-MnO}_2\text{@GO-HT}$  and  $\delta\text{-MnO}_2\text{@GO-HT}$  are larger than that in pure  $\delta\text{-MnO}_2$ , demonstrating that the presence of GO facilitates the generation of oxygen vacancy species [29,41]. Particularly, the mild preparation conditions of  $\delta\text{-MnO}_2\text{@GO-HT}$  favored the construction of defect sites and oxygen adsorption. Therefore,  $\delta\text{-MnO}_2\text{@GO-HT}$  has the best

HCHO removal performance and the abundant  $\text{O}_{\text{ads}}$  plays a crucial role in efficient HCHO oxidation.

Additionally, HCHO-TPD tests were performed to investigate the HCHO adsorption/desorption properties of the four catalysts. As shown in Fig. 4d, HCHO started to desorb around 50 °C, with peak intensities observed at 98 °C, 107 °C, 94 °C and 97 °C for  $\delta\text{-MnO}_2\text{-RT}$ ,  $\delta\text{-MnO}_2\text{@GO-HT}$ ,  $\delta\text{-MnO}_2\text{-HT}$  and  $\delta\text{-MnO}_2\text{@GO-HT}$ , respectively. The higher the peak temperature, the easier it is to adsorb HCHO. Notably, the peak temperature of  $\delta\text{-MnO}_2\text{@GO-HT}$  catalysts was higher than that of  $\delta\text{-MnO}_2$  catalysts, indicating that the modification of GO promoted the



**Fig. 5.** (a) HCHO removal efficiency and (b) corresponding CO<sub>2</sub> concentration as a function of time over various  $\delta\text{-MnO}_2$  samples (HCHO concentration = 100 ppm, N<sub>2</sub> as balance gas, RH = 50%, GHSV = 72 L/g<sub>cat</sub>·h). In-situ DRIFTS spectra over (c)  $\delta\text{-MnO}_2\text{-RT}$ , (d)  $\delta\text{-MnO}_2\text{@GO-HT}$ , (e)  $\delta\text{-MnO}_2\text{-HT}$  and (f)  $\delta\text{-MnO}_2\text{@GO-HT}$  in a flow of N<sub>2</sub> + H<sub>2</sub>O for 30 min and followed by N<sub>2</sub> + HCHO for 30 min at room temperature.



adsorption of HCHO by the catalyst. The CO<sub>2</sub> spectra in Fig. S8 represent the CO<sub>2</sub> generation during the temperature programming process, and the integral area under the two curves reflects the relative content of CO<sub>2</sub> converted by HCHO. The integral area was in the following order:  $\delta\text{-MnO}_2\text{@GO-RT}$  ( $3.15 \times 10^{-7}$ ) >  $\delta\text{-MnO}_2\text{@GO-HT}$  ( $1.34 \times 10^{-7}$ ) >  $\delta\text{-MnO}_2\text{-HT}$  ( $1.15 \times 10^{-7}$ ) >  $\delta\text{-MnO}_2\text{-RT}$  ( $8.59 \times 10^{-8}$ ). A large amount of HCHO was oxidized into CO<sub>2</sub> over  $\delta\text{-MnO}_2\text{@GO-RT}$  even in the absence of oxygen, confirming the abundant and available oxygen species on its surface.

Previous studies have demonstrated that adsorbed water molecules and the ROS are involved in the replenishment of surface -OH groups consumed during HCHO oxidation, but most of these studies have focused on reactions conducted in the presence of oxygen [29,42]. In Fig. 5a, the HCHO removal efficiency of  $\delta\text{-MnO}_2\text{@GO-RT}$  remained close to 100% and stable for nearly 200 min in the absence of oxygen, which is the best performance among the four catalysts. Therefore, it was inferred that  $\delta\text{-MnO}_2\text{@GO-RT}$  can utilize the adsorbed water for the catalytic oxidation of HCHO.

To further investigate the changes in the functional groups on the catalyst surface during the oxygen-free reaction, in situ DRIFTS experiments were performed by introducing H<sub>2</sub>O + N<sub>2</sub> and HCHO + N<sub>2</sub> for HCHO oxidation over the four catalysts at room temperature (Figs. 5c–5f). During the first 30 min, an increase in the absorption bands associated with  $\delta(\text{OH})$  stretching vibration and bending vibration of the -OH group of adsorbed water (located around 3450 cm<sup>-1</sup> and 1655 cm<sup>-1</sup> respectively) was observed in the infrared spectra of all four catalysts (Figs. 5c–5f) [43]. The bands of  $\delta(\text{OH})$  stretching vibration were relatively narrow and well defined in  $\delta\text{-MnO}_2\text{-HT}$  and  $\delta\text{-MnO}_2\text{@GO-HT}$  but broader in  $\delta\text{-MnO}_2\text{-RT}$  and  $\delta\text{-MnO}_2\text{@GO-RT}$ . The abundant defect sites of amorphous  $\delta\text{-MnO}_2$  enhanced the adsorption of water. The intensity of  $\delta(\text{OH})$  bands in  $\delta\text{-MnO}_2\text{@GO}$  catalysts (Figs. 5d and 5f) was stronger than that in  $\delta\text{-MnO}_2$  catalysts (Figs. 5c and 5e), indicating that the modification of GO further promoted the adsorption and activation of water. Upon the introduction of HCHO into the system, prominent bands corresponding to formate species (around 2836 cm<sup>-1</sup>, 1564 cm<sup>-1</sup>, 1346 cm<sup>-1</sup>) appeared in the infrared spectra (Figs. 5c–5f) [44,45]. The increase in formate species bands coincided with a decrease in  $\delta(\text{OH})$  bands around 3600 cm<sup>-1</sup>, suggesting that the surface -OH group plays a pivotal role in the oxidation of HCHO to formate. Only one formate band, identified as the asymmetric  $\nu_{\text{as}}(\text{OCO})$  stretch near 1564 cm<sup>-1</sup>, was observed in Figs. 5e and 5f, suggesting that less formate accumulated on the surface of the catalysts prepared at room temperature. The  $\delta\text{-MnO}_2\text{@GO-RT}$  showed the minimum consumption of surface -OH group, which can be attributed to the capture of water molecules by defects and the conversion of adsorbed water into surface -OH group by abundant surface ROS. As a result, the surface -OH group consumed in the reaction are replenished. Therefore,  $\delta\text{-MnO}_2\text{@GO-RT}$  can directly activate the surface adsorbed water to form abundant surface -OH, leading to excellent performance in catalytic oxidation of HCHO.

### 3.4. Mechanism of catalytic HCHO oxidation

To further investigate the decomposition process of HCHO and to identify the conversion pathway of intermediates on the surface of  $\delta\text{-MnO}_2$ , in-situ DRIFTS experiments were conducted at room temperature with 100 ppm HCHO/air inlet flow. Previous research has confirmed that HCHO molecules adsorbed on the surface of the catalyst are converted to formates, which are subsequently oxidized by -OH groups to form CO<sub>2</sub> and H<sub>2</sub>O. The spectra in Figs. 6a–6d showed four bands of formate species around 1348 cm<sup>-1</sup>, 1387 cm<sup>-1</sup>, 1589 cm<sup>-1</sup>, and 2831 cm<sup>-1</sup>, confirming that formate is the primary surface intermediate resulting from the partial oxidation of HCHO [46,47]. The spectrum of  $\delta\text{-MnO}_2\text{@GO-RT}$  (Fig. 6b) showed relatively low intensity bands of formate species and the absence of a band around 1464 cm<sup>-1</sup> attributed to DOM species. The DOM on the surface of  $\delta\text{-MnO}_2\text{@GO-RT}$  is rapidly converted to formate without accumulation, and

$\delta\text{-MnO}_2\text{@GO-RT}$  exhibited enhanced capacity for oxidation of formate species compared to other catalysts. In Figs. 6c and 6d, two bands around 3300 cm<sup>-1</sup> and 3600 cm<sup>-1</sup> observed for  $\delta\text{-MnO}_2\text{-HT}$  and  $\delta\text{-MnO}_2\text{@GO-HT}$  are attributed to adsorbed water  $\delta(\text{OH})$  and formed surface -OH groups  $\nu(\text{OH})$ , respectively [29,47,48]. The band intensities of formed surface -OH groups are initially increased and then gradually declined, meaning the activation of adsorbed water molecules into -OH groups for formate oxidation [49]. Two bands around 1049 cm<sup>-1</sup> are ascribed to carbonate and the reduction indicated that the decomposition of carbonate is faster than its formation on the surface of catalysts [46]. Only a broad band around 3300 cm<sup>-1</sup> of adsorbed water  $\delta(\text{OH})$  is observed over  $\delta\text{-MnO}_2\text{-RT}$  and  $\delta\text{-MnO}_2\text{@GO-RT}$  (Figs. 6a and 6b). The adsorbed water intensity of  $\delta\text{-MnO}_2\text{@GO-RT}$  is lower than that of  $\delta\text{-MnO}_2\text{-RT}$ , demonstrating that adsorbed water molecules can be rapidly activated and consumed during HCHO catalytic oxidation.

Based on the characterization test results, we proposed a possible reaction mechanism of HCHO oxidation over  $\delta\text{-MnO}_2\text{@GO-RT}$  (Fig. 6e). The in-situ growth of  $\delta\text{-MnO}_2$  nanoparticles on the GO nanosheets increases the specific surface area and exposes more active sites, which promotes the adsorption capacity of oxygen and water molecules and improves the activation efficiency of the ROS and the -OH groups on the surface. According to the XPS results,  $\delta\text{-MnO}_2\text{@GO-RT}$  has the highest concentration of oxygen vacancies on the catalyst surface. Moreover, HCHO-TPD results revealed the involvement of numerous surface ROS in the catalytic oxidation of HCHO. Therefore, the reaction mechanism of HCHO oxidation can be described as follows: firstly, HCHO molecules are rapidly adsorbed on the catalyst surface by hydrogen bonding with surface -OH groups. Subsequently, molecular oxygen is captured by surface oxygen vacancies and excited to the ROS (O<sub>2</sub>, O<sup>•</sup>), which further oxidize the adsorbed HCHO to DOM. DOM is then rapidly oxidized to formates, carbonates, and CO<sub>2</sub>. In the absence of oxygen, water molecules can be directly captured by the surface oxygen vacancy and activated to form surface -OH groups. The surface -OH group and the ROS well cooperated to promote catalytic oxidation of HCHO.

To demonstrate the suitability of this strategy,  $\delta\text{-MnO}_2\text{@GO-RT-I}$  catalyst was synthesized using industrial GO powder via the similar method to  $\delta\text{-MnO}_2\text{@GO-RT}$ . Its HCHO removal performance was evaluated in a low-concentration HCHO gas stream close to the actual environment. As shown in Fig. 6f, the HCHO removal efficiency of the  $\delta\text{-MnO}_2\text{@GO-RT-I}$  catalyst was almost maintained at nearly 98% during the 40 h test. And the CO<sub>2</sub> concentration is stable at 4–5 ppm (Fig. S9). Compared with the  $\delta\text{-MnO}_2\text{@GO-RT}$  catalyst, the  $\delta\text{-MnO}_2\text{@GO-RT-I}$  has simpler preparation processes using trace industrial GO, which substantially reduces the cost. Therefore,  $\delta\text{-MnO}_2\text{@GO-RT-I}$  is expected to be applied in large-scale industrial applications.

## 4. Conclusion

In summary, the 2D coralloid hierarchical pores  $\delta\text{-MnO}_2\text{@GO}$  were synthesized through an in-situ growth strategy. The  $\delta\text{-MnO}_2\text{@GO-RT}$  exhibited terrific HCHO removal efficiency of 100% and stability, which was far superior to the MnO<sub>x</sub> catalysts reported in the previous literature. The interaction between GO and MnO<sub>2</sub> effectively prevented particle agglomeration of  $\delta\text{-MnO}_2$ , thus maximizing the exposure of active sites. The catalysts synthesized at room temperature have more active sites than those synthesized by the hydrothermal method. The dispersive and abundant catalytic active sites greatly reduced the diffusion limitation, improved the oxygen and water adsorption and activation capacity. The plentiful ROS and -OH groups of  $\delta\text{-MnO}_2\text{@GORT}$  well cooperated to accelerate the catalytic oxidation of HCHO and maintain the remarkable catalytic activity and stability toward HCHO degradation. This study provides an effective method to maximize the exposure of catalytic sites and rationally design the efficient industrial catalysts for indoor HCHO elimination.

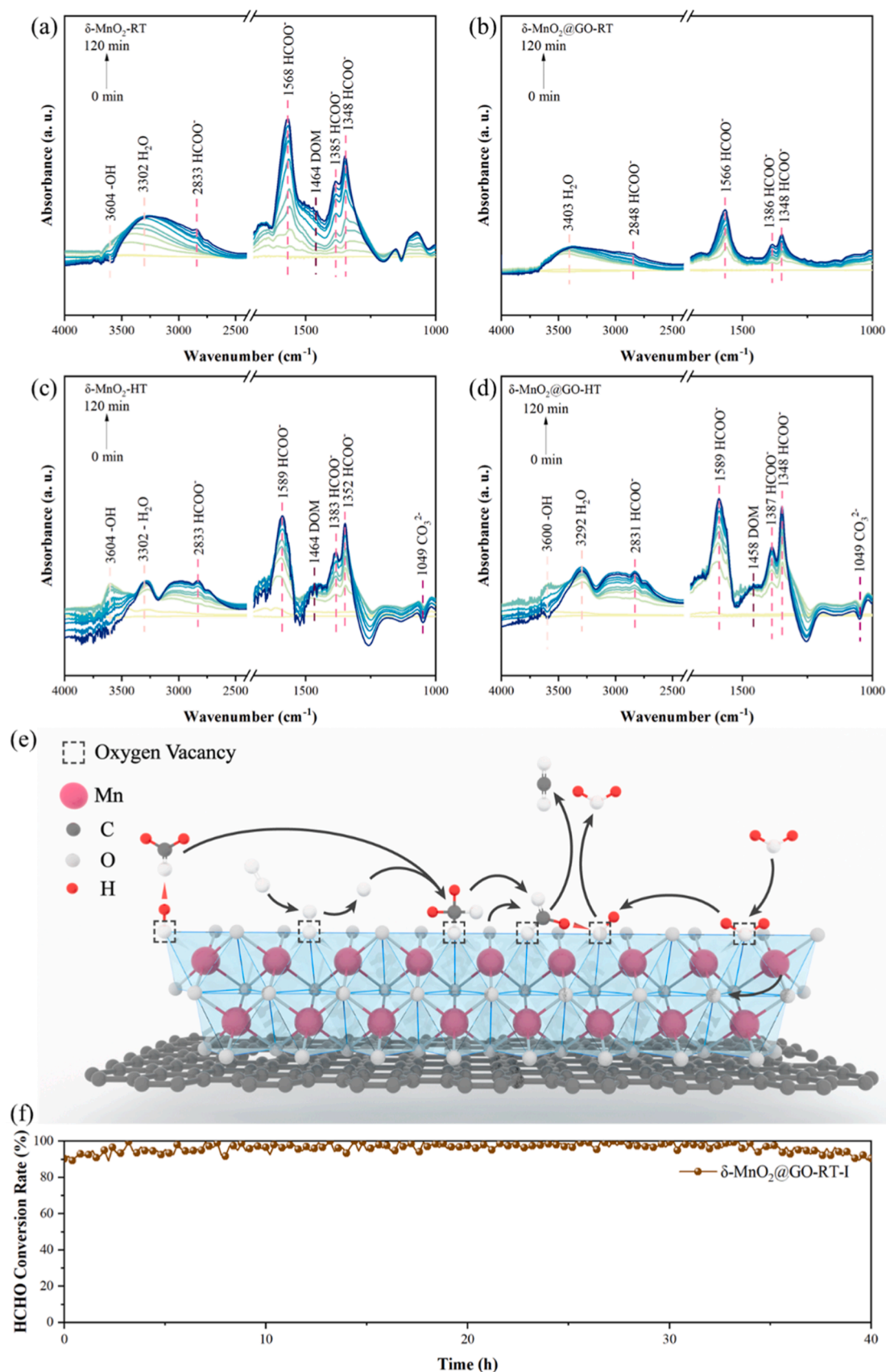


**Fig. 6.** In-situ DRIFTS spectra of (a)  $\delta\text{-MnO}_2$ -RT, (b)  $\delta\text{-MnO}_2$ @GO-RT, (c)  $\delta\text{-MnO}_2$ -HT and (d)  $\delta\text{-MnO}_2$ @GO-HT exposed to a flow of HCHO at room temperature. (e) Possible mechanism of HCHO oxidation on  $\delta\text{-MnO}_2$ @GO-RT at room temperature. (f) Stability test over  $\delta\text{-MnO}_2$ @GO-RT-I (HCHO concentration = 10 ppm, air as balance gas, temperature  $\sim 25^\circ\text{C}$ , RH = 50%, GHSV = 72  $\text{L/g}_{\text{cat}}\cdot\text{h}$ ).

## CRediT authorship contribution statement

H. H., and Y. L. conceived the research idea and designed the experiments. Y. L. performed the experiments, analyzed data, and wrote the original manuscript. T. D. and J. J. participated in writing and revising the article. Y. L. and T. D. are contributed equally to this article. All authors contributed to the development of this article. All authors have approved the final version of the article.

## Declaration of Competing Interest

The authors declare that they have no known competing financial interests or personal relationships that could have appeared to influence the work reported in this paper.

## Data availability

No data was used for the research described in the article.

## Acknowledgments

This work was supported by the National Natural Science Foundation of China (22076224 and 22276223).

## Supporting information

Catalyst synthesis, characterization, computational methods, activity test, summary of economic benefits for different catalysts in the literature, and other supporting figures and tables (PDF).

## Appendix A. Supporting information

Supplementary data associated with this article can be found in the online version at [doi:10.1016/j.apcatb.2023.123322](https://doi.org/10.1016/j.apcatb.2023.123322).

## References

- [1] Y. Zhang, Y. Wang, R. Xie, H. Huang, M.K.H. Leung, J. Li, D.Y.C. Leung, Photocatalytic oxidation for volatile organic compounds elimination: from fundamental research to practical applications, *Environ. Sci. Technol.* 56 (2022) 16582–16601.
- [2] D. Hu, Y. Tobon, A. Agostini, B. Grosselin, Y. Chen, C. Robin, A. Yahyaoui, P. Colin, A. Mellouki, V. Daële, Diurnal variation and potential sources of indoor formaldehyde at elementary school, high school and university in the Centre Val de Loire region of France, *Sci. Total Environ.* 811 (2022), 152271.
- [3] W. Wei, C. Howard-Reed, A. Persily, Y. Zhang, Standard formaldehyde source for chamber testing of material emissions: model development, experimental evaluation, and impacts of environmental factors, *Environ. Sci. Technol.* 47 (2013) 7848–7854.
- [4] J. Shi, R. Zhang, Z. Mi, S. Lyu, J. Ma, Engineering a sustainable chrome-free leather processing based on novel lightfast wet-white tanning system towards eco-leather manufacture, *J. Clean. Prod.* 282 (2021), 124504.
- [5] S. Wang, Q. Han, Z. Wei, Y. Wang, L. Deng, M. Chen, Formaldehyde causes an increase in blood pressure by activating ACE/AT1R axis, *Toxicology* 486 (2023), 153442.
- [6] O.S.a.H. Administration, Part 1910.1048(c) Permissible Exposure Limit (PEL), in: D.o. Labor (Ed.), Federal Register, 2013, pp. 1910.1048(c).
- [7] Y. Le, D. Guo, B. Cheng, J. Yu, Bio-template-assisted synthesis of hierarchically hollow SiO<sub>2</sub> microtubes and their enhanced formaldehyde adsorption performance, *Appl. Surf. Sci.* 274 (2013) 110–116.
- [8] J. Yuan, P. Xu, J. Wang, W. Zhang, J. Zhou, A. Lai, L. Wang, Experimental study on the removal of formaldehyde by plasma-catalyst, *IOP Conf. Ser.: Earth Environ. Sci.* 435 (2020), 012004.
- [9] Y. Qin, Z. Wang, J. Jiang, L. Xing, K. Wu, One-step fabrication of TiO<sub>2</sub>/Ti foil annular photoreactor for photocatalytic degradation of formaldehyde, *Chem. Eng. J.* 394 (2020), 124917.
- [10] J. Zhang, R. Shan, H. Xiao, S. Hu, Z. Sheng, X. Qin, Y. Zhang, L. Wang, J. Li, C. Zhang, Electronic modification by transitional metal dopants to tune the oxidation activity of Pt-CeO<sub>2</sub>-based catalysts, *Environ. Sci. Technol.* 56 (2022) 17331–17340.
- [11] C. Duan, M. Meng, H. Huang, H. Ding, Q. Zhang, Z. Lin, S. Huang, C. Chen, M. He, Effect of calcination temperature on the structure and formaldehyde removal performance at room temperature of Cr/MnO<sub>2</sub> catalysts, *Res. Chem. Intermed.* 48 (2022) 2705–2720.
- [12] J. Guo, C. Lin, C. Jiang, P. Zhang, Review on noble metal-based catalysts for formaldehyde oxidation at room temperature, *Appl. Surf. Sci.* 475 (2019) 237–255.
- [13] D. Chen, G. Zhang, M. Wang, N. Li, Q. Xu, H. Li, J. He, J. Lu, Pt/MnO<sub>2</sub> nanoflowers anchored to boron nitride aerogels for highly efficient enrichment and catalytic oxidation of formaldehyde at room temperature, *Angew. Chem. Int. Ed.* 60 (2021) 6377–6381.
- [14] J. Gong, S. Rong, X. Wang, Y. Zhou, Critical review of catalytic degradation of formaldehyde via MnO<sub>2</sub>: from the perspective of process intensification, *J. Clean. Prod.* 377 (2022), 134242.
- [15] D.C. Fang, J.Y. Zheng, C.B. Han, W.K. Zhao, Y.G. Lu, B.C. Sun, L. Sun, X. Wang, H. Yan, Electro-injection-enhanced catalytic formaldehyde degradation based on conductive MnO cellulose aerogels at room temperature, *Appl. Catal. B Environ.* 334 (2023), 122837.
- [16] X. Zhou, Y. Liu, C. Song, J. Liu, A study on the formaldehyde emission parameters of porous building materials based on adsorption potential theory, *Build. Environ.* 106 (2016) 254–264.
- [17] Z. Han, C. Wang, X. Zou, T. Chen, S. Dong, Y. Zhao, J. Xie, H. Liu, Diatomite-supported birnessite-type MnO<sub>2</sub> catalytic oxidation of formaldehyde: preparation, performance and mechanism, *Appl. Surf. Sci.* 502 (2020), 144201.
- [18] J. Ye, M. Zhou, Y. Le, B. Cheng, J. Yu, Three-dimensional carbon foam supported MnO<sub>2</sub>/Pt for rapid capture and catalytic oxidation of formaldehyde at room temperature, *Appl. Catal. B Environ.* 267 (2020), 118689.
- [19] S. Ullah, Y. Liu, M. Hasan, W. Zeng, Q. Shi, X. Yang, L. Fu, H.Q. Ta, X. Lian, J. Sun, R. Yang, L. Liu, M.H. Rummeli, Direct synthesis of large-area Al-doped graphene by chemical vapor deposition: advancing the substitutionally doped graphene family, *Nano Res.* 15 (2021) 1310–1318.
- [20] J. Xu, D. Li, Y. Chen, L. Tan, B. Kou, F. Wan, W. Jiang, F. Li, Constructing sheet-on-sheet structured graphitic carbon nitride/reduced graphene oxide/layered MnO<sub>2</sub> ternary nanocomposite with outstanding catalytic properties on thermal decomposition of ammonium perchlorate, *Nanomaterials* 7 (2017) 450.
- [21] L. Li, Z. Du, S. Liu, Q. Hao, Y. Wang, Q. Li, T. Wang, A novel nonenzymatic hydrogen peroxide sensor based on MnO<sub>2</sub>/graphene oxide nanocomposite, *Talanta* 82 (2010) 1637–1641.
- [22] Z. Hu, Y. Zhao, J. Liu, J. Wang, B. Zhang, X. Xiang, Ultrafine MnO<sub>2</sub> nanoparticles decorated on graphene oxide as a highly efficient and recyclable catalyst for aerobic oxidation of benzyl alcohol, *J. Colloid Interface Sci.* 483 (2016) 26–33.
- [23] W.S.H. Jr, R.E. Offeman, Preparation of graphitic oxide, *J. Am. Chem. Soc.* 80 (1958), 1339–1339.
- [24] G. Zhu, W. Zhu, Y. Lou, J. Ma, W. Yao, R. Zong, Y. Zhu, Encapsulate alpha-MnO<sub>2</sub> nanofiber within graphene layer to tune surface electronic structure for efficient ozone decomposition, *Nat. Commun.* 12 (2021) 4152.
- [25] R. Fang, X. Huang, Xa Luo, Y. Sun, Z. Liu, L. Ao, F. Dong, H. Huang, Excellent stability for catalytic oxidation formaldehyde over defective δ-MnO<sub>2</sub> nanoparticles at room temperature, *J. Environ. Chem. Eng.* 11 (2023), 109064.
- [26] Y. Li, J. Wang, Y. Zhang, M.N. Banis, J. Liu, D. Geng, R. Li, X. Sun, Facile controlled synthesis and growth mechanisms of flower-like and tubular MnO<sub>2</sub> nanostructures by microwave-assisted hydrothermal method, *J. Colloid Interface Sci.* 369 (2012) 123–128.
- [27] L. Yang, S. Cheng, J. Wang, X. Ji, Y. Jiang, M. Yao, P. Wu, M. Wang, J. Zhou, M. Liu, Investigation into the origin of high stability of δ-MnO<sub>2</sub> pseudo-capacitive electrode using operando Raman spectroscopy, *Nano Energy* 30 (2016) 293–302.
- [28] R.A. El-Mallawany, Theoretical and experimental IR spectra of binary rare earth tellurite glasses—1, *Infrared Phys.* 29 (1989) 781–785.
- [29] J. Ji, X. Lu, C. Chen, M. He, H. Huang, Potassium-modulated δ-MnO<sub>2</sub> as robust catalysts for formaldehyde oxidation at room temperature, *Appl. Catal. B Environ.* 260 (2020), 118210.
- [30] X. Min, M. Guo, L. Liu, L. Li, J.N. Gu, J. Liang, C. Chen, K. Li, J. Jia, T. Sun, Synthesis of MnO<sub>2</sub> derived from spent lithium-ion batteries via advanced oxidation and its application in VOCs oxidation, *J. Hazard. Mater.* 406 (2021), 124743.
- [31] B. Bai, Q. Qiao, H. Arandiyar, J. Li, J. Hao, Three-dimensional ordered mesoporous MnO<sub>2</sub>-supported Ag nanoparticles for catalytic removal of formaldehyde, *Environ. Sci. Technol.* 50 (2016) 2635–2640.
- [32] C.I. Wang, A.P. Periasamy, H.T. Chang, Photoluminescent C-dots@RGO probe for sensitive and selective detection of acetylcholine, *Anal. Chem.* 85 (2013) 3263–3270.
- [33] F. Colson, D.A. Barlow, Statistical method for modeling Knudsen diffusion in nanopores, *Phys. Rev. E* 100 (2019), 062125.
- [34] B. Besser, H.A. Tajiri, G. Mikolajczyk, J. Mollmer, T.C. Schumacher, S. Odenbach, R. Glaser, S. Kroll, K. Rezwan, Hierarchical porous zeolite structures for pressure swing adsorption applications, *ACS Appl. Mater. Interfaces* 8 (2016) 3277–3286.
- [35] K. Li, C. Chen, H. Zhang, X. Hu, T. Sun, J. Jia, Effects of phase structure of MnO<sub>2</sub> and morphology of δ-MnO<sub>2</sub> on toluene catalytic oxidation, *Appl. Surf. Sci.* 496 (2019), 143662.
- [36] Y. Boyjoo, G. Rochard, J.-M. Giraudon, J. Liu, J.-F. Lamonier, Mesoporous MnO<sub>2</sub> hollow spheres for enhanced catalytic oxidation of formaldehyde, *Sustain. Mater. Technol.* 20 (2019), e00091.
- [37] H. Lin, D. Chen, H. Liu, X. Zou, T. Chen, Effect of MnO<sub>2</sub> crystalline structure on the catalytic oxidation of formaldehyde, *Aerosol Air Qual. Res.* 17 (2017) 1011–1020.
- [38] Y. Xie, Y. Yu, X. Gong, Y. Guo, Y. Guo, Y. Wang, G. Lu, Effect of the crystal plane figure on the catalytic performance of MnO<sub>2</sub> for the total oxidation of propane, *CrystEngComm* 17 (2015) 3005–3014.
- [39] R. Li, L. Zhang, S. Zhu, S. Fu, X. Dong, S. Ida, L. Zhang, L. Guo, Layered δ-MnO<sub>2</sub> as an active catalyst for toluene catalytic combustion, *Appl. Catal. A* 602 (2020), 117715.
- [40] J. Liu, H. Su, Y. Hu, C. Gong, J. Lu, D. He, W. Zhu, D. Chen, X. Cao, J. Li, S. Gligorovski, Y. Luo, Highly efficient degradation of sulfur-containing volatile



- organic compounds by amorphous MnO<sub>2</sub> at room temperature: implications for controlling odor pollutants, *Appl. Catal. B Environ.* 334 (2023), 122877.
- [41] J. Liu, H. Wang, L. Wang, P. Jian, X. Yan, Phase-dependent catalytic performance of MnO<sub>2</sub> for solvent-free oxidation of ethylbenzene with molecular oxygen, *Appl. Catal. B Environ.* 305 (2022), 121050.
- [42] J. Wang, P. Zhang, J. Li, C. Jiang, R. Yunus, J. Kim, Room-temperature oxidation of formaldehyde by layered manganese oxide: effect of water, *Environ. Sci. Technol.* 49 (2015) 12372–12379.
- [43] Z. Han, C.I. Wang, X. Zou, T. Chen, S. Dong, Y. Zhao, J. Xie, H. Liu, Diatomite-supported birnessite-type MnO<sub>2</sub> catalytic oxidation of formaldehyde: preparation, performance and mechanism, *Appl. Surf. Sci.* 502 (2020), 144201.
- [44] Q. Jin, Y. Shen, Y. Cai, L. Chu, Y. Zeng, Resource utilization of waste V<sub>2</sub>O<sub>5</sub>-based deNO<sub>x</sub> catalysts for hydrogen production from formaldehyde and water via steam reforming, *J. Hazard. Mater.* 381 (2020), 120934.
- [45] K. Zha, W. Sun, Z. Huang, H. Xu, W. Shen, Insights into high-performance monolith catalysts of Co<sub>3</sub>O<sub>4</sub> nanowires grown on nickel foam with abundant oxygen vacancies for formaldehyde oxidation, *ACS Catal.* 10 (2020) 12127–12138.
- [46] F. Liu, S. Rong, P. Zhang, L. Gao, One-step synthesis of nanocarbon-decorated MnO<sub>2</sub> with superior activity for indoor formaldehyde removal at room temperature, *Appl. Catal. B Environ.* 235 (2018) 158–167.
- [47] Y. Xu, J. Dhainaut, G. Rochard, J.-P. Dacquin, A.-S. Mamede, J.-M. Giraudon, J.-F. Lamonier, H. Zhang, S. Royer, Hierarchical porous  $\epsilon$ -MnO<sub>2</sub> from perovskite precursor: application to the formaldehyde total oxidation, *Chem. Eng. J.* 388 (2020), 124146.
- [48] T. Dong, J. Ji, L. Yu, P. Huang, Y. Li, Z. Suo, B. Liu, Z. Hu, H.J.J.A. Huang, Tunable interfacial electronic Pd–Si interaction boosts catalysis via accelerating O<sub>2</sub> and H<sub>2</sub>O activation, *JACS Au* 3 (2023) 1230–1240.
- [49] L. Miao, J. Wang, P. Zhang, Review on manganese dioxide for catalytic oxidation of airborne formaldehyde, *Appl. Surf. Sci.* 466 (2019) 441–453.